Research Article | Vol. 30, No. 24 / 21 Nov 2022 / Optics Express 43384
Optics EXPRESS

Surface astigmatism correction using segmented freeform surfaces for a progressive addition lens

RISHENG XIA,[1,2] YAOYAO FU,[1] KE MA,[1] SIYUN CHEN,[1] JIANYOU PAN,[1] CHAOHUI ZHOU,[1] HAIHUA FENG,[1] JIA QU,[1,2,†*] AND YIYU LI[1,2,3,†]

[1]School of Optometry and Ophthalmology, Wenzhou Medical University, Zhejiang 325000, China
[2]National Engineering Research Center of Ophthalmology & Optometry, China
[3]liyiyu@wmu.edu.cn
[†]Co-corresponding authors.
[*]jqu@wmu.edu.cn

Abstract: The undesired distribution of irregular surface astigmatism (SA) on the freeform surface has been the major concern of progressive addition lens (PAL) design. Herein, we proposed a segmented freeform surface (SFS) construction method, which relies on the lines of curvature to rule the surface segmentation and then eliminates the difference between principal curvatures to correct the SA. Based on ray tracing and numerical simulation results, the SFS-PAL design has superior performance in image quality within a dynamic field of view over the conventional freeform PAL. To verify the feasibility and the real performance of the new design, we used the diamond turning method with a fast tool servo to realize the rapid prototyping, and then used injection molding for the mass production of the high-quality SFS-PALs.

1. Introduction

Progressive addition lenses (PAL) are multifocal ophthalmic lenses and are widely accepted among consumers to remedy presbyopia [1]. The functional areas of PAL include a distance zone for distance vision, a near zone with addition power for near vision, and an intermediate corridor providing a variable focus. The functional areas are flanked to either side by blending zones with gradient curvatures which induce irregular surface astigmatism (SA) or unwanted cylinder oriented at an oblique axis, leading to the blurred image and geometrical distortion which are the primary drawback of PAL and the major concern of lens designers for decades.

Either side or both sides of PAL can be multifocally functionalized. Several design methods including the direct analytical method [2,3] and the indirect numerical method [4–6] have been proposed for the freeform surface construction to provide the desired surface power distribution in the functional areas. However, as a trade-off, the undesired SA with a magnitude close to the addition power remains in the blending zones, a fact first pointed out by Minkwitz [7]. This limitation imposes on PAL design a functional minimization problem combined with optimal weight functions for the target surface power (or mean curvature) and SA [8,9].

For SA-free correction, an unexplored option is using segmented freeform surface (SFS) in the blending zones. This option will challenge the lens design from at least three aspects. First, the desired distribution of spherical addition power should be best unchanged after surface segmentation. Second, SA should be suppressed or eliminated in the blending zone without inducing additional imaging defect that is visually intolerable. Third, the proposed SFS should be best compatible with the existing high-precision surface processing technology. In this work, we will address all the issues and explore the approach to the fabrication of high-performance SFS-PALs.

#476678 https://doi.org/10.1364/OE.476678
Journal © 2022 Received 27 Sep 2022; revised 25 Oct 2022; accepted 25 Oct 2022; published 9 Nov 2022

Optics EXPRESS

2. Design concept

The conventional PAL design uses a smooth freeform surface described as a function $z = Z(x, y)$ with its continuous derivatives everywhere. Zernike basis functions expressed in terms of powers of x and y can be used to represent the surfaces [10], so the first-order and second-order derivatives can be algebraically calculated. At each point on the surface, the orthogonal principal curvatures κ_1 and κ_2 [11], representing the maximum and the minimum plane curvatures respectively in the normal planes, are given by

$$\kappa_1 = H - \sqrt{H^2 - K} \tag{1}$$

$$\kappa_2 = H + \sqrt{H^2 - K} \tag{2}$$

$$H = \frac{EN + GL - 2FM}{2(EG - F^2)},\ K = \frac{LN - M^2}{EG - F^2}$$

$$E = 1 + Z_x^2,\ F = Z_x Z_y,\ G = 1 + Z_y^2$$

$$L = \frac{Z_{xx}}{\sqrt{1 + Z_x^2 + Z_y^2}},\ M = \frac{Z_{xy}}{\sqrt{1 + Z_x^2 + Z_y^2}},\ N = \frac{Z_{yy}}{\sqrt{1 + Z_x^2 + Z_y^2}}$$

where, H and K are mean curvature and Gaussian curvature, respectively. The directions of normal planes containing principal curvatures are determined by

$$\alpha_i = \arctan\left(-\frac{M - \kappa_i F}{N - \kappa_i G}\right),\quad i = 1,\ 2 \tag{3}$$

The principal curvatures contribute to the surface spherical powers called high power $P_1(x, y)$ and low power $P_2(x, y)$, respectively, and measured in diopters as

$$P_i(x, y) = (n - 1)\kappa_i(x, y),\quad i = 1,\ 2 \tag{4}$$

where n is the refractive index of lens material. The difference between high power and low power is defined as SA

$$SA(x, y) = |P_1(x, y) - P_2(x, y)| \tag{5}$$

Here, a conventional freeform PAL was first designed for myopia of −1.50 diopters suffering from presbyopia. The lens was composed of a front base curve of 4.00 diopters and a back prescription curve of −5.50 diopters with the required addition power. The refractive index of 1.60 and lens central thickness of 3.5 mm are used in all the designs. The far reference point at which PAL provides distance vision prescription is located 8 mm above the geometrical center. The near reference point providing a near vision prescription is located 11 mm below the geometrical center and 2 mm displaced toward the nasal side.

2.1. Axial orientation of SA

The variational-difference numerical method [8] combined with the weight functions and the target distribution of surface power suggested in Ref. [9] was utilized to solve the posterior freeform surfaces of the conventional PALs as shown in Fig. 1. The distributions of spherical power and SA were calculated based on the surface geometry by using Eq. (1)-(5). The arrows displayed with SA represent the axial orientation of SA (AOSA), and also indicate the direction of the normal plane of high power.

In the blending zone occupied by the high-level SA, the AOSA features a pattern of gradual tilt toward the central area of the lens. By setting a starting point at the circular aperture of 50 mm in diameter and following the local direction of AOSA to find the next sampling point at a constant spacing of 0.02 mm, a curved trajectory recording the variation of AOSA can be obtained.

Optics EXPRESS

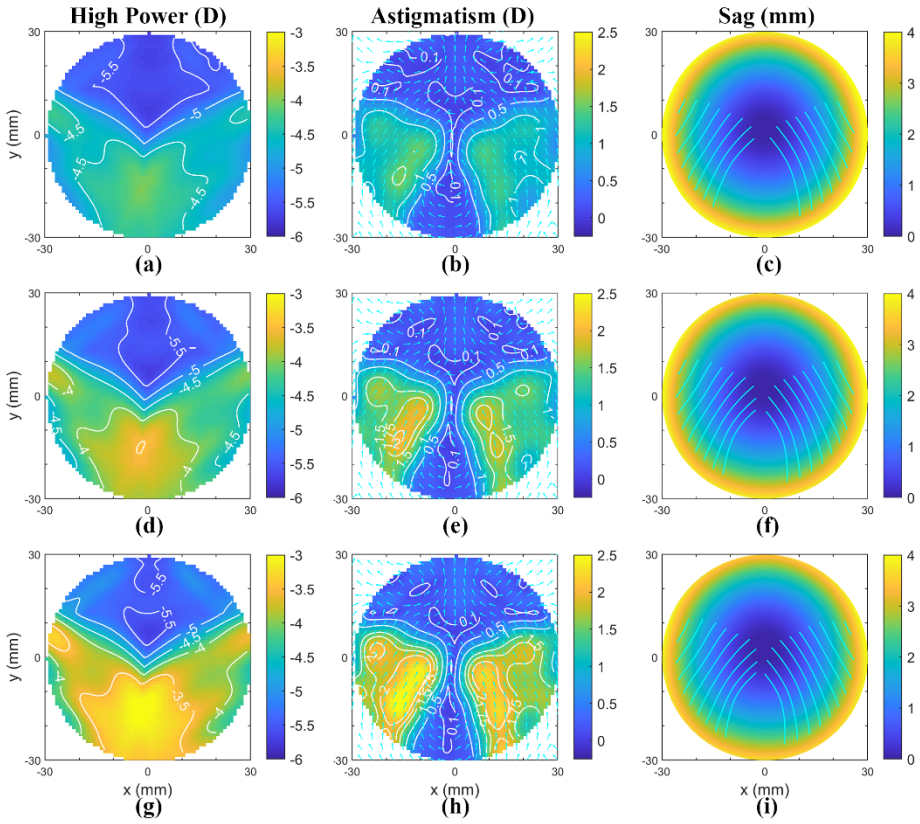

Fig. 1. Power maps and sag profiles of the posterior freeform surfaces of conventional PALs design. The arrows displayed in SA maps represent the AOSA. The lines of curvature for SP = 3.5 mm are depicted in the sag profiles. (a)-(c) Addition power of 1.50 D; (d)-(f) addition power of 2.00 D; (g)-(i) addition power of 2.50 D.

In differential geometry, a standard expression of the trajectories of AOSA is the line of curvature which is a curve embedded in the surface tangent to a principal direction. Hereinafter, we refer to the trajectories of AOSA as the line of curvature.

Figure 1 shows the lines of curvature attached to the sag profiles. All the lines of curvature were calculated within the area of SA higher than 0.75 diopters to avoid any umbilical line or points at which the solutions will become indeterminate [12]. These umbilical points are already known in PAL design and are normally distributed along the principle line that connects the far reference point and the near reference point.

The lines of curvature will be used to define the central lines of segmented surfaces discussed in the next section. The lines of curvature can hardly intersect each other as long as the starting points are lateral displaced. The distance between two adjacent lines of curvature can be a measure of segment pitch (SP) which is not a constant, so an average value is used for the approximate expression of SP in the following discussion. The higher the required addition power in design, the more area will be occupied by blending zones with an increased level of SA, which results in more lines of curvature as well as segmented surfaces to be constructed.

Optics EXPRESS

2.2. Segmentation and reconfiguration of freeform surface

The original surface in the blending zones was divided up into several segments by considering the line of curvature as the central line of each segmented part, so that the SA can be treated independently for each segment. A straightforward method is to force the two principal curvatures to be equal for SA-free correction according to Eq. (5). This method has been illustrated in Fig. 2(a). A point P on the freeform surface is chosen at a line of curvature. At this point, the surface has a normal direction $\overline{N}$. The normal plane is orthogonal to the lines of curvature, thus cutting the surface to give the original plane curve SS' possessing the curvature of κ_2 and the curvature center of C_S. The plane curve SS' is going to be replaced by a new curve TT' which is tangent at point P with curve SS' in the normal plane. To correct the local SA, the new curve TT' should have the same curvature as κ_1 and the curvature center of C_T. In this way, the SA in the surrounding area close to point P can be suppressed.

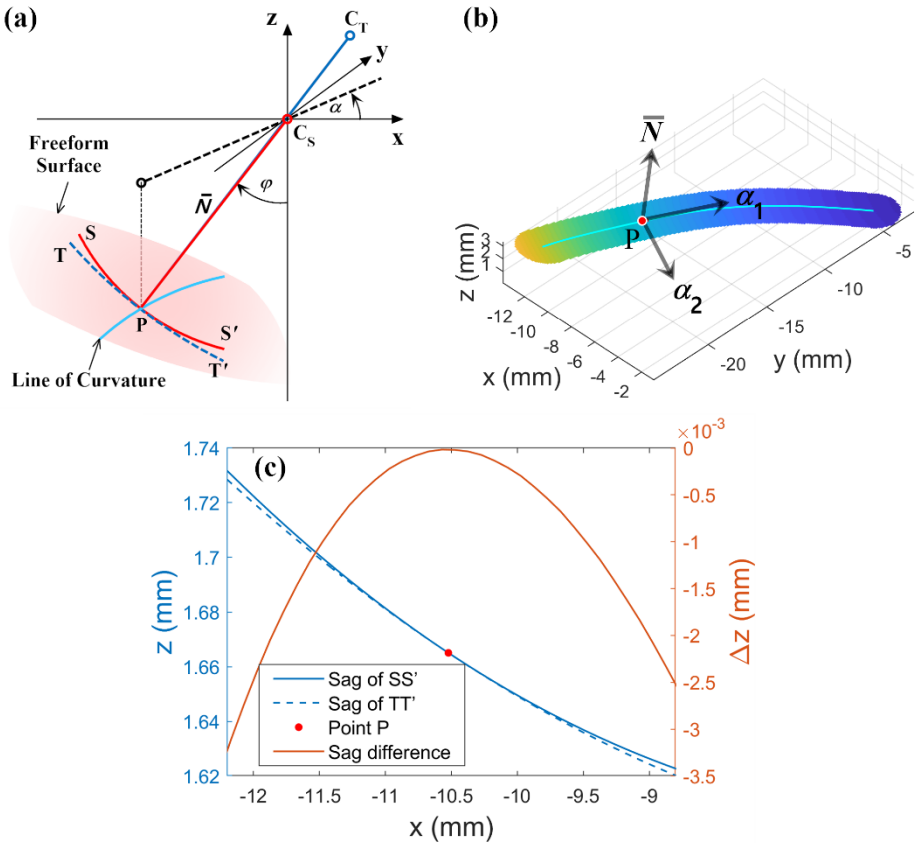

Fig. 2. Construction of the segmented freeform surface. (a) At point P on the original freeform surface, a new plane curve TT' with the curvature of κ_1 is generated to replace the original plane curve SS' of curvature κ_2 in the normal plane. The normal plane has the normal direction $\overline{N}$ and is orthogonal to the line of curvature; (b) a segmented freeform surface was constructed with SP = 3.5 mm for SA correction. The line of curvature starting at point (−11, −25) was used as the central line; (c) sag profiles of plane curves as well as the sag difference in the case of point P chosen in Fig. 2(b).

The difference between plane curve SS' and TT' in the z-direction, referred to as the sag difference, can be calculated as follows. Supposing the curvature center C_S is located on the

Optics EXPRESS

coordinate origin, we can have

$$\cos\varphi = z_P\kappa_2,\ \sin\alpha = \frac{y_P\kappa_2}{\sin\varphi},\ \cos\alpha = \frac{x_P\kappa_2}{\sin\varphi} \tag{6}$$

where, φ is the angle of normal direction concerning the z-coordinate. The coordinate of the curvature center C_T can be represented by

$$\begin{aligned} x_T &= -\sin\varphi\cos\alpha\left|\frac{1}{\kappa_1}-\frac{1}{\kappa_2}\right| \\ y_T &= -\sin\varphi\sin\alpha\left|\frac{1}{\kappa_1}-\frac{1}{\kappa_2}\right| \\ z_T &= -\cos\varphi\left|\frac{1}{\kappa_1}-\frac{1}{\kappa_2}\right| \end{aligned} \tag{7}$$

where, α is the azimuthal angle. For any point with coordinates $(x_i,\ y_i)$ in the normal plane, the sag difference between plane curves SS' and TT' can be estimated as

$$\Delta z(x_i,\ y_i) = \left[\sqrt{\frac{1}{{\kappa_1}^2}-(x_i-x_T)^2-(y_i-y_T)^2}+z_T\right]-\sqrt{\frac{1}{{\kappa_2}^2}-{x_i}^2-{y_i}^2} \tag{8}$$

So, the sag profile of the new plane curve TT' within the segment can be obtained by adding the calculated sag difference to the original plane curve SS'. This operation is repeated for each point along the lines of curvature. Finally, the collection of the newly constructed plane curves constitutes the desired segmented surface as shown in Fig. 2(b). The scale of sag difference is a few microns largely determined by the value of SP and the SA to be corrected.

Following the same approach to the sag profile optimization in each segment, the whole profile of the calculated sag difference within the blending zone was obtained and shown in Fig. 3(a). To avoid any abrupt change in the geometric topography, a smooth transition was applied to the junction region between adjacent segments, so that the following surface finishing process such as high-precision diamond machining [13,14] can be performed.

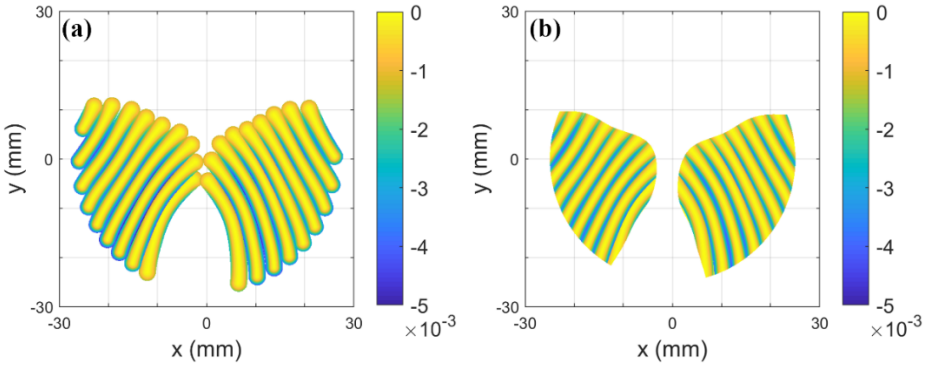

Fig. 3. Profile of sag difference $\Delta z(x_i, y_i)$ obtained (a) before smooth transition operation and (b) after smooth transition operation for SFS-PAL design with addition power of 2.00 D and SP = 3.5 mm. The calculated sag difference outside of the region where SA is lower than 1.00 D is out of consideration.

To perform the smooth transition, only the calculated sag difference with an absolute magnitude less than 2.5 μm in Fig. 3(a) was preserved, leading to the gaps between adjacent segments. Then a built-in fillmissing function in MATLAB (R2018a, MathWorks) was utilized to fill these gaps using spline interpolation, so that the adjacent segments can be joined smoothly with continuous

Optics EXPRESS

boundary transition to give the final result as shown in Fig. 3(b). At last, the combination of the original freeform surface $Z(x, y)$ and the smoothed calculated sag difference $\Delta z(x_i,\ y_i)$ gave rise to the configuration of SFS $Z_S(x, y)$.

Zernike polynomials are not suitable to represent the SFS anymore, so the method of point cloud data with a high-density sampling of surface topography is employed. The partial derivatives of SFS in two dimensions were estimated by using a numerical gradient algorithm such as the built-in gradient function in MATLAB. The sampling point spacing was 0.05 mm in a Cartesian mesh for the high accuracy of numerical calculation. The same Cartesian mesh has been employed for the calculation of power profiles and sag profiles from Fig. 1 to Fig. 3. Surface powers of SFS were calculated by using Eq. (1)-(5) and shown in Fig. 4. By comparing to Fig. 1, the high-power distributions almost remain unchanged after the generation of SFS, while the low-power distributions of SFS in the blending zones become similar to the high-power distributions, therefore realizing the correction of SA. The only defect is the remaining high-level SA in the junction regions between adjacent segmented parts which is mainly caused by surface smoothing operation.

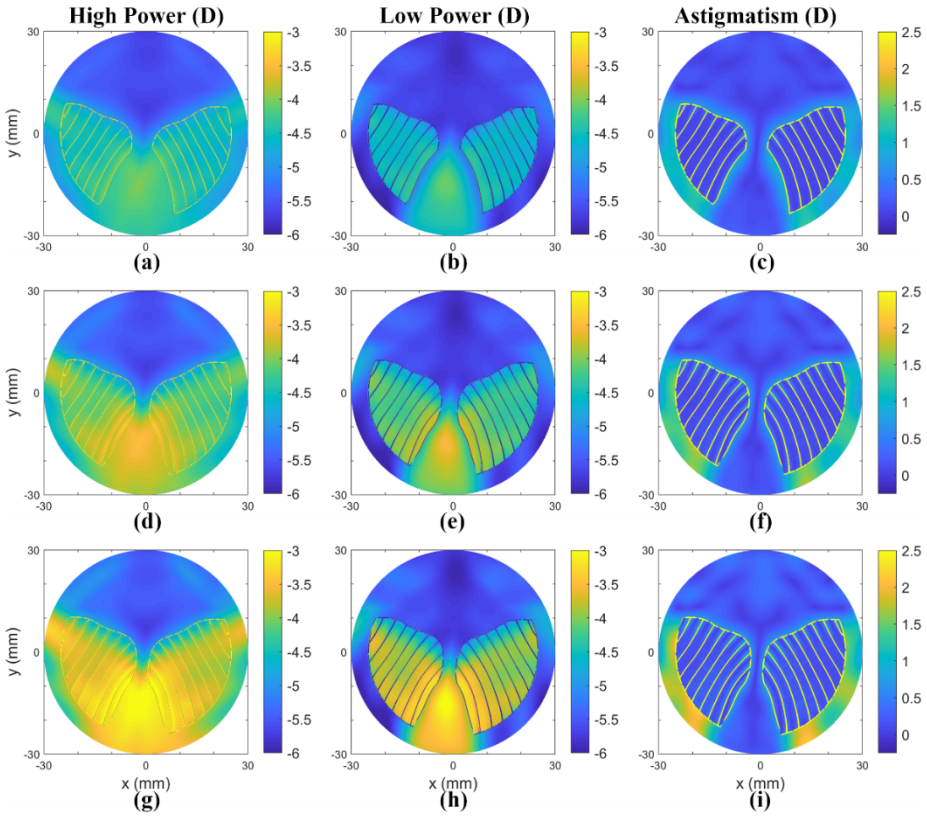

Fig. 4. Calculated power maps of SFS-PAL with SP = 3.5 mm and (a)-(c) addition power of 1.50 D; (d)-(f) addition power of 2.00 D; (g)-(i) addition power of 2.50 D.

3. Simulation and discussion

The image performance was simulated in a lens-eye system [15,16] composed of PAL, aperture stop, and the rotation center of the eyeball. There is an object point with a definite location in the lens-eye system for each gaze direction within the dynamic field of view which is defined as

Optics EXPRESS

the volume formed by the conjugate points of fovea for all possible gaze directions, so the ray tracing from the object point to the image space of PAL can give the emergent wavefront for image quality evaluation.

3.1. Reverse ray tracing for the determination of object point

In the lens-eye system, the origin of coordinates is set at the vertex of the anterior lens surface whose radius curvature is 150 mm. The posterior lens surface can be a conventional freeform surface or the SFS described in Section 2. For each gaze direction, the light path of the chief ray in the image space of PAL can be easily determined by drawing the line from the rotation center of the eye to the point of interest on the posterior lens surface. Then, reverse ray tracing in three dimensions is performed for the chief ray from the posterior lens surface back to the object space of PAL. The object distance is quantified by the reciprocal of the working addition power taking effect at the intersection between the chief ray and SFS. The combination of the object distance and the direction of the chief ray in object space gives the coordinate of the object point. In Fig. 5, there are 18 gaze directions were chosen for simulation. The positions of chief rays on SFS marked as red stars in Fig. 5(a) are evenly arranged with a horizontal spacing of 6 mm and a vertical spacing of 8 mm within the blending zones.

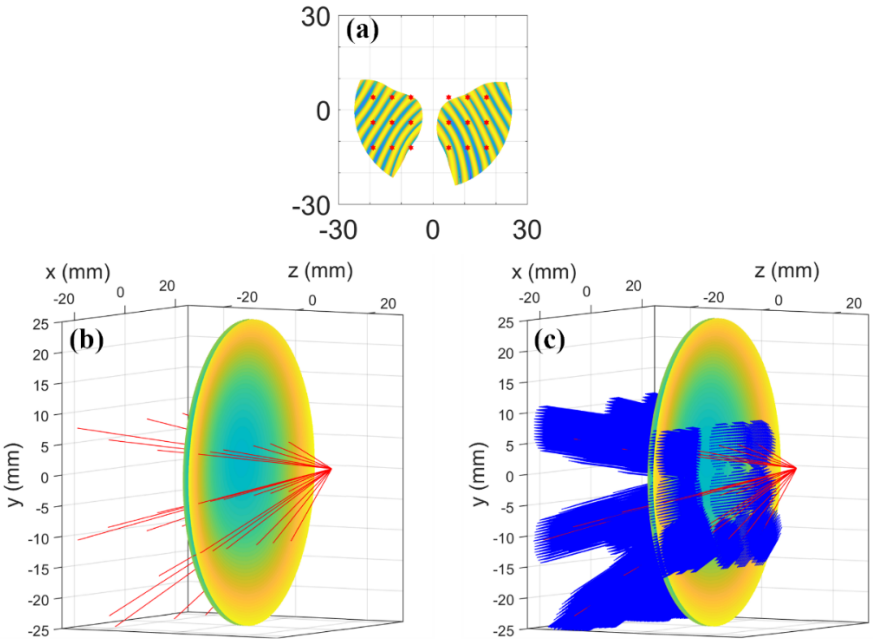

Fig. 5. Three-dimensional ray tracing of PAL. (a) Selected positions of chief rays on the posterior lens surface for the determination of gaze directions; (b) light path of the chief rays traced from the rotation center of eyeball back to object space; (c) high-density ray tracing from object point to image space within the working aperture of 8 mm for each gaze direction.

3.2. Emergent wavefront of PAL for image quality evaluation

For each gaze direction, a large number of rays were traced from the object point through the lens and terminate at the vertex sphere defined by a radius curvature of 24 mm. The center of the vertex sphere coincides with the rotation center of the eyeball. The rays filled in an aperture of 8 mm in diameter to cover the general size of the eye pupil.

Optics EXPRESS

An iteration algorithm was utilized for the ray tracing of the posterior lens surface to determine the incident points on the surface with high accuracy. First, the intersection S_0 of the incident ray with the original freeform surface $Z(x, y)$ was calculated. The point S_1 with the same x and y coordinates as S_0 was estimated by interpolation of the point cloud data of SFS. Then a tangent plane through S_1 was constructed to find the intersection S_2 with the ray, which was generally closer to the SFS than the point S_0. The derivatives of the surface, required for the tangent plane construction, were calculated by the same numerical gradient algorithm for the power map simulation in Fig. 4. This step was repeated until the intersection found on the ray was close enough to the SFS. For practical purposes, the iterative process is terminated when the change in point coordinates between successive approximations is less than 1.0×10^{-10} mm.

The optical path length was calculated for each ray and compared to that of the chief ray to give the emergent wavefront at the vertex sphere as shown in Fig. 6 where the results of simulations are arranged in a rectangular array pattern according to the chief ray locations defined in Fig. 5(a). Both the SFS-PAL and the conventional freeform PAL are employed in lens-eye system simulations for comparison.

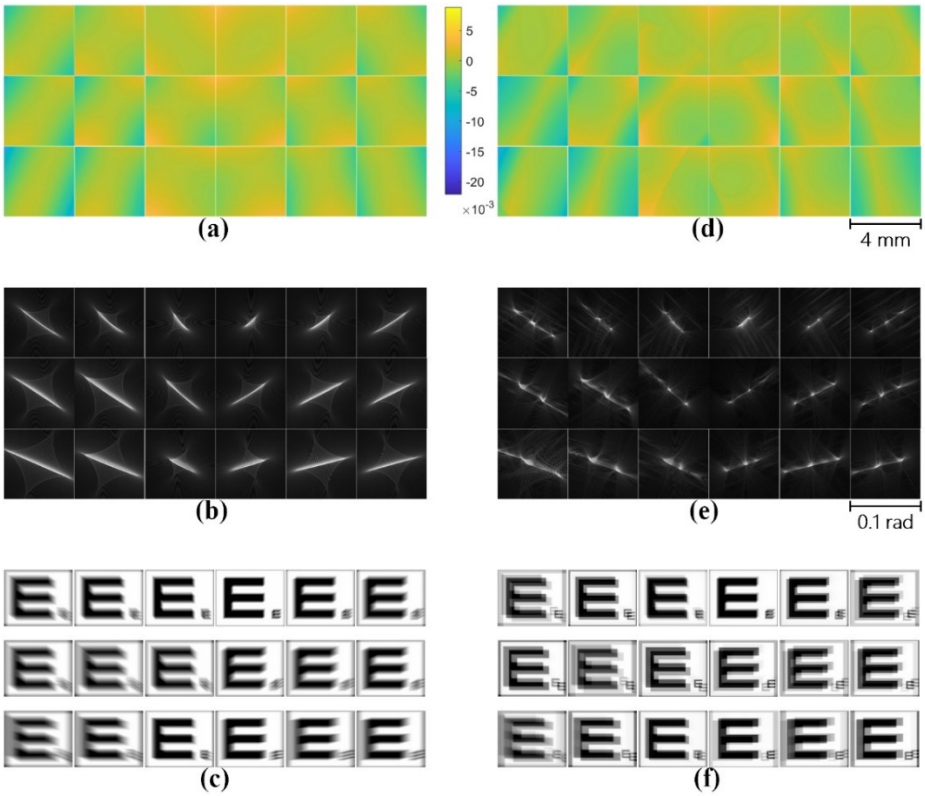

Fig. 6. Image quality evaluation based on the calculated emergent wavefront for PAL design with addition power of 2.00 D. (a) Emergent wavefront, (b) PSF, and (c) image of an extended object simulated for conventional PAL; (d) emergent wavefront, (e) PSF, and (f) image of an extended object simulated for SFS-PAL with SP of 3.5 mm.

The point spread functions (PSFs) shown in Fig. 6, representing the simulation of Fresnel diffraction pattern, were obtained by Fourier transform of the generalized pupil function containing the calculated emergent wavefront within a pupil aperture of 6 mm in diameter. The observation plane was set at the focus of equivalent spheric power of the emergent wavefront. In the case

Optics EXPRESS

of conventional PAL design, the wavefront aberrations especially dominant astigmatism force the intensity distributions of PSFs to be expanded in particular directions, leading to the blurred images of an extended object as shown in Fig. 6(c) which were generated by convolving the PSF with the extended object.

In contrast, SFS-PAL provides segmented emergent wavefronts as long as the SP is smaller than the eye pupil, so the Fresnel diffraction pattern features a series of bright spots with non-uniform intensity distribution. As a consequence, multiple images can be observed simultaneously as shown in Fig. 6(f), while only one dominant image with a quality much better than that of conventional PAL can be expected for each gaze direction. One of the segmented parts of the emergent wavefront, which occupies the largest area of the pupil aperture, contributes to the dominant image. Furthermore, SFS-PALs have superior performance in modulation transfer function as shown in Fig. 7.

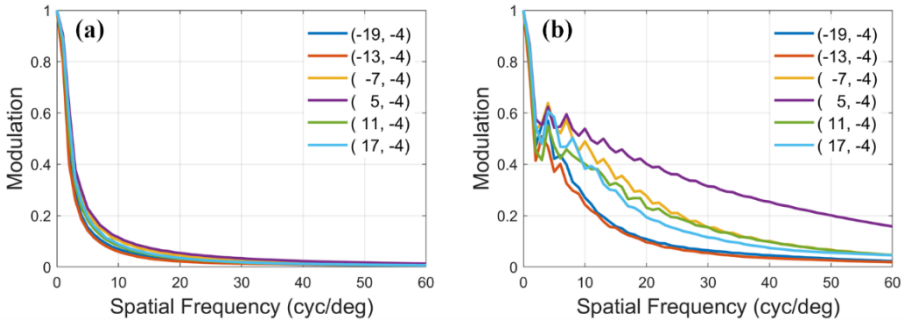

Fig. 7. Calculated MTF of PALs for 6 different gaze directions featured by chief ray positions defined in Fig. 5. (a) conventional PAL; (b) SFS-PAL with SP of 3.5 mm.

3.3. Consideration of segment pitch

Except the dominant image provided by SFS-PAL when gazing through the blending zone, the rest accompanying images behaving like ghost images [17], as shown in Fig. 8, may impair the contrast perceived especially when a small SP is employed. It is suggested to use a large SP comparable to the regular pupil diameter so that MTF and image quality can be improved. However, the shortcoming of a larger SP is that it brings visible changes in geometrical topography between adjacent segments, therefore requiring robust dynamic response capacity with high accuracy in the following surface processing.

3.4. Wavering phenomenon of the dominant image

Within the dynamic field of view, the line-of-sight is controlled by eye rotation to go through any point on SFS. During the scanning of line-of-sight, the intensity distribution of PSF featured by the aligned bright spots varies continuously as the change of the working area of SFS determined by the chief ray. As shown in Fig. 9, when the scanning of line-of-sight was performed in the x direction by a lateral step of 0.5 mm for the chief ray position on SFS, the dominant image and the background ghost image switched their positions regularly, leading to the wavering phenomenon of image.

In practice, in the case of a dynamic field of view without head rotation, the eye is tracking an unfixed or dynamic target. The wavering phenomenon may be unnoticeable or tolerable as the change or the movement of the target itself. The wavering phenomenon will be most noticeable only in the case of tracking a fixed static target during the head rotation and eye rotation, which is not a common case for PAL wearers.

Optics EXPRESS

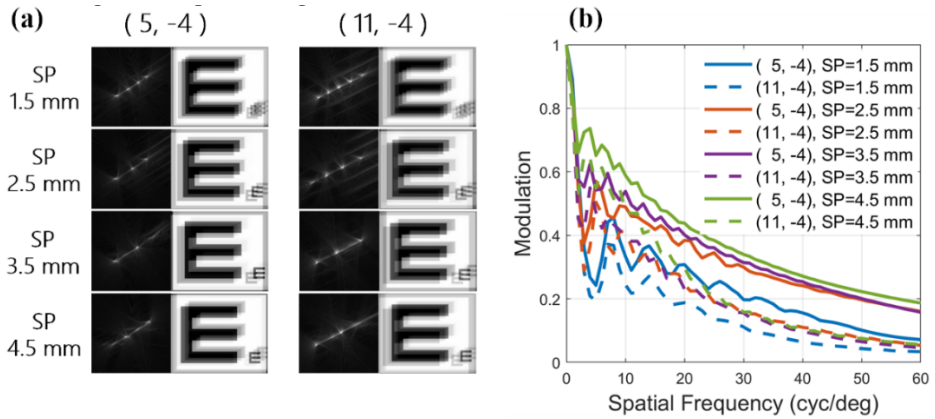

Fig. 8. Impact of SP on the performance of SFS-PAL with addition power of 2.00 D. (a) PSF and image of an extended object simulated for gaze direction determined by chief ray position at (5, -4) (left column) and (11, -4) (right column) on the posterior lens surface; (b) calculated MTF for the two gaze directions.

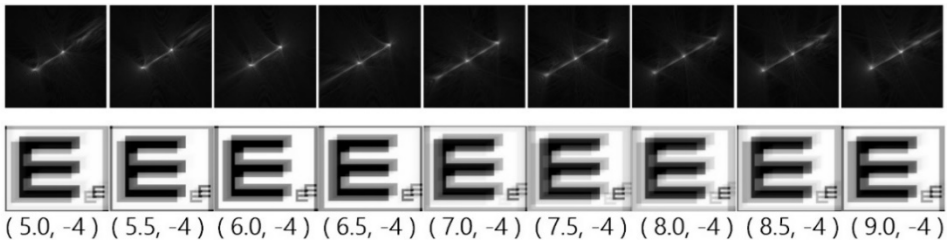

Fig. 9. PSFs and simulated images of SFS-PAL designed with an addition power of 2.00 D and SP = 3.5 mm as the line-of-sight scans in the x direction. The coordinates indicate the chief ray positions on the SFS.

4. Manufacture and measurement

As a proof-of-concept, the SFS-PALs were fabricated by using diamond turning based on a self-developed computer-numerically controlled (CNC) freeform generator [18] with up to 3 axes of positioning capability (2 linear and 1 angular). As a deterministic fabrication method, diamond turning directly reproduces the programmed geometric tool paths, which makes it suitable for the fast prototyping of PALs.

We have developed proprietary software using MATLAB programming to transfer the 3D point cloud of SFS with high-frequency freeform features into a standard format of CNC data for surface machining. The SFS $Z_S(x, y)$, represented by a point cloud with a regular grid pitch of 0.05 mm as introduced in Section 2, is interpolated over a new polar mesh grid within an aperture of 60 mm in diameter. The grid point elements are equally spaced along the radial direction with an incremental size of 10 μm and are circumferentially spaced with a fixed angular increment of 0.15°. Therefore, the whole surface is well described with up to 7.2×10^6 supporting points utilized for tool path construction. Any control node in the tool path is calculated by linear interpolation with four adjacent supporting points. The tool path calculation costs the computation time of 2 minutes based on a desktop computer equipped with an Intel i7 processor of 1.8 GHz clock frequency.

The freeform generator used a polycrystalline diamond tool for rough cutting with a depth of 0.3 mm and a natural diamond tool for the surface finishing with a cutting depth of 0.1 mm to

Optics EXPRESS

fabricate SFS on the back side of a lens blank made of CR-39. The two-tool configuration is mounted on a fast tool servo (FTS) unit which provides the required stroke of 0.5 mm for lens surfacing. Limited by the working bandwidth and the tracking error of tool motion, the FTS operated under a constant spindle speed of 80 rpm and a feed rate of 0.8 mm/min.

The polishing process, required for the fabrication of conventional PALs, will remove not only the tool marks but also the intended micro-structure, so it is harmful to the topography maintenance of SFS and should be skipped. Therefore, after surface finishing, the unpolished SFS-PALs were directly subject to hard coating to reduce the surface scattering caused by tool marks and to improve the lens transparency for the following power measurement.

A lens inspection system (Rotlex, Contest Plus) operating on the Moiré deflectometer, was used to measure the power profiles of SFS-PALs within a sub-aperture of 8 mm in diameter. The measured multiple sub-apertures were arranged in a hexapolar pattern, as shown in Fig. 10, and combined for power map demonstration. During the measurement, a three-axis linear translation stage was used to support the precision motion of the lens mount and the positioning of sub-apertures. Due to the limited physical space provided by the inspection system for the translation of the lens mount, only the lower half part of the lens, including the region of segmented surfaces, can be covered in measurement.

In the experiment, four SFS-PALs with different SPs were fabricated. The measured addition power at the near reference point is very close to 2.00 D in all the cases. The SA has been suppressed obviously in the blending zones especially for SFS design with larger SP, except the residual SA distributed in the junction regions of segments due to the surface smoothing operation as predicted in Fig. 4. The hard layers which were not conformally coated may partly contribute to the residual SA. It should be noted that the defect caused by tool marks left on the SFSs, even covered by the hard coating, are still visible and disturb the measured results of power profiles. The inertia and the limited bandwidth of FTS may also account for the deviation of the measurement from the theoretical design.

To improve the form accuracy and eliminate the defect caused by tool marks, injection molding as a formative manufacturing process was used for the mass production of SFS-PALs. The mold insert with high-quality surface finishing within a clear aperture of 75 mm, as shown in Fig. 11(a), was straightforwardly generated using ultra-precision diamond turning machining. The material used for the lens was polycarbonate. The process conditions including molten temperature, mold temperature, injection pressure, and cooling time were optimized during the preliminary runs on an electric injection molding machine (FANUC ROBOSHOT Models, α-S150iA). The surface segmentations, which are almost invisible on the appearance of the lens produced by injection molding, can generate a unique intensity distribution on the background, as shown in Fig. 11(b), under the illumination of a point source. The measured power profile shows consistency with the simulation results.

Optics EXPRESS

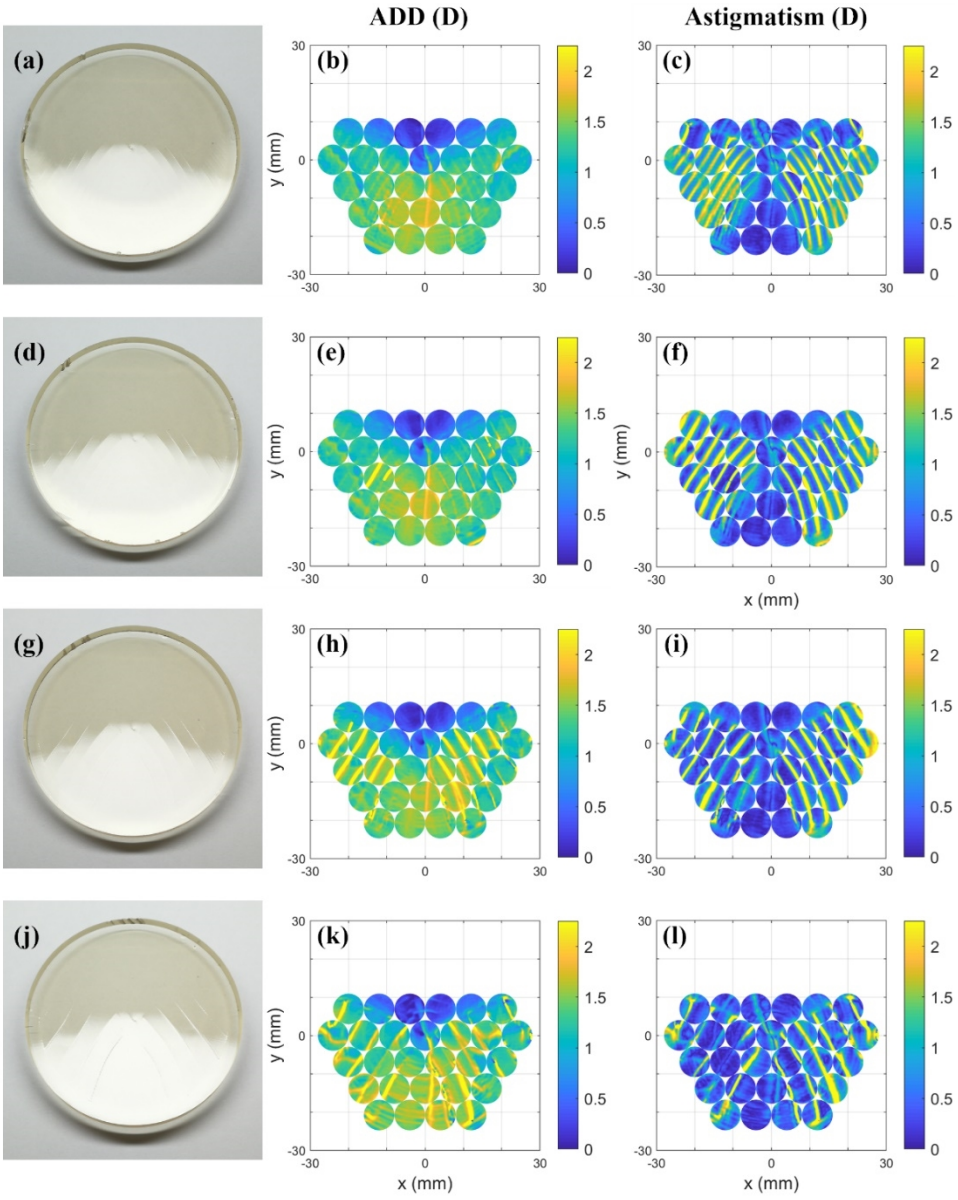

Fig. 10. Measured power profiles of the unpolished and hard layer coated SFS-PALs using sub-aperture stitching method. The size of the sub-aperture is 8 mm in diameter. ADD profile was obtained by subtracting the spheric component of prescription from the measured high-power map. (a)~(c) SP = 2.5 mm; (d)~(f) SP = 3.5 mm; (g)~(i) SP = 4.5 mm; (j)~(l) SP = 6.0 mm.

Optics EXPRESS

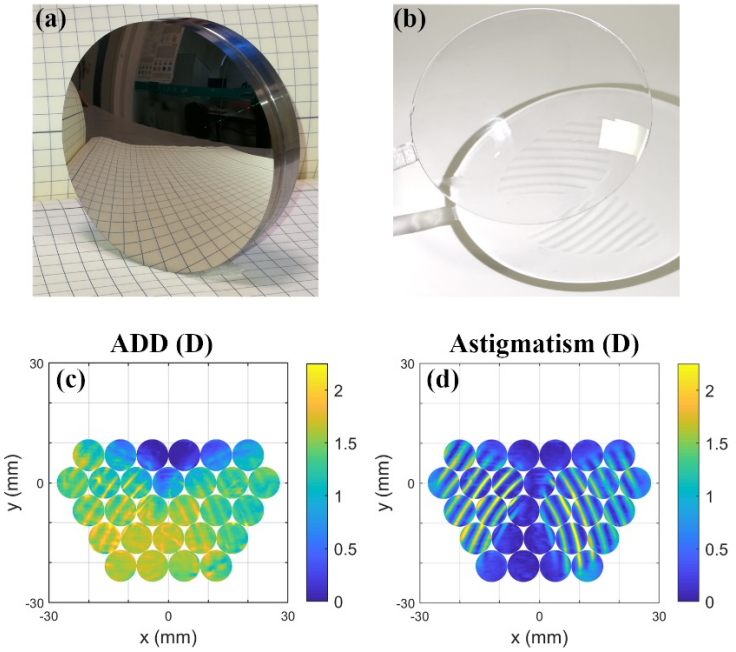

Fig. 11. Injection molding of SFS-PALs designed with addition power of 2.00 D and SP = 3.5 mm. (a) Mold insert fabricated by single-point diamond turning; (b) molded SFS-PALs; the measured distribution of (c) addition power and (d) SA.

5. Conclusion

The design, simulation, and fabrication of SFS-PALs were addressed in this paper. The lines of curvature, as a new property of conventional PAL, were utilized to guide the segmentation process of freeform surfaces in the blending zones. The surface segmentation offers the opportunity for the re-optimization of the sag profile within each segment to correct the SA without altering the distribution of progressive addition power. The simulations of the lens-eye system demonstrated the superior performance of SFS-PAL in imaging quality over the conventional PAL except for the wavering phenomenon of the dominant image.

The SFS-PALs were manufactured by direct diamond turning based on a self-developed hardware platform. The freeform generator enables fast prototyping however with limited forming accuracy and a major issue of tool marks. Sub-aperture measurement and stitching method of power profiles were utilized to verify the feasibility of the manufacturing process. As a promising solution to high-volume manufacturing, injection molding was proposed to produce high-quality SFS-PALs with the help of ultra-precision mold fabrication.

Funding. National Natural Science Foundation of China (61775171).

Acknowledgments. The authors wish to thank Zengshi Su for the valuable discussion about the injection molding process and thank Jiangwei Shu and Yan Gu for sharing the ultra-precision lathe for the fabrication of mold inserts.

Disclosures. The authors declare no conflicts of interest.

Data availability. Data underlying the results presented in this paper are not publicly available at this time but may be obtained from the authors upon reasonable request.

Optics EXPRESS

References

1. J. E. Sheedy, "Progressive addition lenses-matching the specific lens to patient needs," Optometry - Journal of the American Optometric Association **75**(2), 83–102 (2004).
2. J. T. Winthrop, "Progressive addition spectacle lens," U.S. patent 4 861 153 (29 August 1989).
3. J. T. Winthrop, "Progressive addition spectacle lens," U.S. patent 5 123 725 (23 June 1992).
4. J. Loos, G. Greiner, and H. P. Seidel, "A variational approach to progressive lens design," Computer-Aided Design **30**(8), 595–602 (1998).
5. J. Wang, R. Gulliver, and F. Santosa, "Analysis of a variational approach to progressive lens design," SIAM J. Appl. Math. **64**(1), 277–296 (2003).
6. J. Wang and F. Santosa, "A numerical method for progressive lens design," Math. Models Methods Appl. Sci. **14**(04), 619–640 (2004).
7. G. Minkwitz, "On the surface astigmatism of a fixed symmetrical aspheric surface," Math. Models Methods Appl. Sci. **10**(3), 223–227 (1963).
8. W. Jiang, W. Z. Bao, Q. L. Tang, H. Q. Wang, and L. Zhu, "A variational-difference numerical method for designing progressive-addition lenses," Computer-Aided Design **48**, 17–27 (2014).
9. Y. Li, W. Huang, H. Feng, and J. Chen, "Customized design and efficient machining of astigmatism-minimized progressive addition lens," Chin. Opt. Lett. **16**(11), 113302 (2018).
10. Y. Li, R. Xia, J. Chen, H. Feng, Y. Yuan, D. Zhu, and C. Li, "Freeform surface of progressive addition lens represented by Zernike polynomials," Proc. SPIE **9683**, 96830W (2016).
11. E. Abbena, S. Salamon, and A. Gray, *Modern Differential Geometry of Curves and Surfaces with Mathematica* (CRC Press, 2006).
12. S. Barbero and M. M. González, "Admissible surfaces in progressive addition lenses," Opt. Lett. **45**(20), 5656–5659 (2020).
13. L. Zhang, W. Zhou, N. J. Naples, and A. Y. Yi, "Fabrication of an infrared Shack–Hartmann sensor by combining high-speed single-point diamond milling and precision compression molding processes," Appl. Opt. **57**(13), 3598–3605 (2018).
14. L. Zhu, Z. Li, F. Fang, S. Huang, and X. Zhang, "Review on fast tool servo machining of optical freeform surfaces," Int J Adv Manuf Technol **95**(5-8), 2071–2092 (2018).
15. J. Alonso, J. Gómez-Pedrero, and J. A. Quiroga, "*Modern Ophthalmic Optics*," (Cambridge University Press, 2019).
16. P. Rojo, S. Royo, J. Ramírez, and I. Madariaga, "Numerical implementation of generalized Coddington equations for ophthalmic lens design," J. Mod. Opt. **61**(3), 204–214 (2014).
17. S. Barbero, A. Bradley, N. López-Gil, J. Rubinstein, and L. Thibos, "Catastrophe optics theory unveils the localized wave aberration features that generate ghost images," Ophthalmic. Physiol. Opt. **42**(5), 1074–1091 (2022).
18. H. Feng, R. Xia, Y. Li, J. Chen, Y. Yuan, D. Zhu, S. Chen, and H. Chen, "Fabrication of freeform progressive addition lenses using a self-developed long stroke fast tool servo," Int. J. Adv. Manuf. Technol. **91**(9-12), 3799–3806 (2017).